Argon collisions with amorphous water ice surfaces

4 **AUTHORS**, INCLUDING:

Kim Bolton
Högskolan i Borås
140 PUBLICATIONS **2,547** CITATIONS

SEE PROFILE

Jan B. C. Pettersson
University of Gothenburg
166 PUBLICATIONS **2,384** CITATIONS

SEE PROFILE

Chemical Physics

Argon collisions with amorphous water ice surfaces

Martina T. Suter [a], Kim Bolton [b], Patrik U. Andersson [a], Jan B.C. Pettersson [a,*]

[a] *Department of Chemistry, Atmospheric Science, Göteborg University, SE-412 96 Göteborg, Sweden*
[b] *School of Engineering, University of Borås, SE-50190, Borås, Sweden*

Abstract

The dynamics of argon atom collisions with amorphous ice surfaces are investigated using molecular beam techniques and molecular dynamics simulations. The formation of an amorphous ice layer on top of crystalline ice at 110 K is shown to have a strong influence on Ar scattering. Compared to crystalline ice, trapping followed by desorption is favoured over inelastic scattering, and a strongly enhanced emission of argon in the backward direction is observed. Molecular dynamics simulation with different types of amorphous and crystalline surfaces are consistent with the experimental data and show that large scale corrugation is required to reproduce the experimental findings. It is concluded that argon scattering can be used to probe changes in surface structure on the nanometer length-scale, while it is relatively insensitive to changes on the molecular level, and it thereby complements other techniques for studies of structural changes of ice surfaces.
© 2006 Elsevier B.V. All rights reserved.

1. Introduction

Condensation of water vapor at temperatures lower than about 130 K results in the formation of amorphous ice. Processes involving amorphous ice have received considerable attention in recent years motivated by fundamental interest and astrochemical applications. Many astrophysical sites experience ideal conditions for forming amorphous ice, including comets [1], icy satellites [2] and interstellar dust [3]. The structure of the amorphous ice surface is likely to have a strong influence on different aspects of gas–ice interactions, including energy transfer at surface impact, adsorption, desorption, surface mobility and bulk diffusion. The surface morphology may also have a strong effect on surface reactivity.

The morphology of ice grown by vapor deposition depends on several parameters, including temperature, deposition rate, and incident angle of the incoming water

molecules [1,4–10]. Highly porous ice is formed at low temperatures, while dosing or annealing at temperatures above 90 K limits porosity [6] and nonporous structures are formed above 120 K [11,12]. Above 140 K, crystallization sets in [1,13]. Background dosing and directed off-normal flows of water molecules produce porous structures at low temperatures, while deposition of a directed water flow in the surface normal direction may produce nonporous films [6–9].

Several experimental techniques have been employed to study surface structure and morphological changes of amorphous ice. For example, temperature-programmed desorption (TPD) has been used to follow structural changes of the ice by measuring the release of trapped gases when ice is heated from low temperature to above 150 K [14,15]. Adsorption of weakly bound methane [12] and carbon tetrachloride [16,17] followed by TPD has been used to follow changes in surface structure and morphology, and TPD of N_2 adsorbed at low temperature has been used to evaluate the apparent surface area and pore volume of amorphous ice [6]. The surface structure and morphological

* Corresponding author. Tel.: +46 31 772 28 28; fax: +46 31 772 3107.
E-mail address: janp@chem.gu.se (J.B.C. Pettersson).

changes of amorphous ice have also been studied by infrared spectroscopy that probed dangling OH bonds at the ice surface and adsorbed molecules [12,18,19]. Low-energy electron-stimulated desorption (ESD) of ions from ice has been used to examine film roughness, phase and growth behavior of vapor-deposited ice films [20–22], and photon-stimulated near-edge X-ray absorption fine structure spectroscopy (PSD-NEXAFS) to study changes in surface morphology in the temperature range 38–147 K [10].

In the present study argon collisions with amorphous water ice surfaces are studied using molecular beam techniques and molecular dynamics (MD) simulations. The main aim is to evaluate the effects of ice structure on the atom–surface collision dynamics. Angular-resolved time-of-flight distributions are measured for an incident kinetic energy of 0.43 eV and an incident angle of 70°, using ice surfaces in the temperature range 110–160 K. The results are compared with MD simulations of Ar collisions with different types of ice surfaces. It is concluded that argon scattering is sensitive to changes in surface structure on the nanometer length-scale, and it thereby complements other techniques for studies of structural changes of ice surfaces. In related previous work, molecular beam studies have been carried out of Ar [23], HCl [24], CO [25] and CO_2 [26] interacting with ice at surface temperatures of 100–190 K. Classical MD simulations of Ar scattering from crystalline ice have also been carried out [23,27,28] and serve as a basis for the present study. In a related recent study, Suter et al. [29] used low-energy elastic helium scattering to follow the onset of surface disorder on crystalline ice.

2. Experimental methods

The molecular beam-surface scattering apparatus used to study Ar collisions with ice surfaces has been described in detail elsewhere [23–26], and is only briefly presented here. A pulsed molecular beam source generated pulses with a repetition frequency of 61 s^{-1}. The pulses were synchronized with a chopper in the second chamber in order to select the central part of each pulse, giving square-wave like beam pulses with a width of 90 μs. A mixture of 5% Ar in He gave a kinetic energy of 0.43 eV. The source pressure was kept at 9 bar and the degree of clustering was negligible at this pressure.

The molecular beam collided with an ice surface in the center of the main scattering chamber. A 12×12 mm graphite surface (Advanced Ceramics Corp., grade ZYB, 0.8° spread of the z-axis) was used as a substrate for ice build-up. The sample can be cooled by liquid nitrogen and heated by irradiation giving a surface temperature range of 100–750 K with fluctuations of less than ±0.1 K. The flux from the ice surface is detected by a differentially pumped quadrupole mass spectrometer (QMS) that is rotatable around the ice surface. Angular resolved time-of-flight measurements with a resolution of ≤±1° can be performed in the plane defined by the beam and the surface

normal. Ar$^+$ ions generated by electron bombardment in the QMS were mass selected and thereafter detected by pulse-counting and stored on a multi-channel-scaler with a dwell time of 10 μs.

Ice surfaces were built on the graphite substrate by deposition of water vapor, which was introduced into the cylindrical chamber through a leak valve. The initial build-up of ice was performed at a surface temperature of 150 K and the water vapor pressure around the surface was adjusted to give a build-up rate of 2 monolayers/s (ML/s), which produces stable crystalline ice [23,29]. Crystalline ice I exists in two forms, cubic and hexagonal ice [30,31], of which the hexagonal phase is the most stable form at all temperatures, but often cubic ice is kinetically favoured [30,31]. The relatively fast deposition rate used for ice build-up in this study makes it likely that the produced crystalline ice is cubic. The surface structures of the two phases are, however, very similar. The ice layer produces interference of scattered light from a diode laser that is reflected from the surface, and the effect was used to measure the layer thickness [23,32]. About 1000 ML of ice were initially built up before the Ar beam was turned on. During molecular beam exposure, the water vapor around the surface was either maintained or turned off, which enabled us to perform scattering experiments with both amorphous and crystalline ice. The amorphous ice surface was grown on the initially formed crystalline ice by water deposition at temperatures lower than 130 K.

3. Molecular dynamics simulation methods

3.1. Potential energy surface

The potential energy surface (PES) used to simulate Ar scattering from ice has been described previously [23,27]. The rigid H_2O molecules interactions are represented by TIP4P potentials [33], which have been successful in simulating water systems under a variety of conditions [34,35]. The Ar–ice interaction is described by Lennard-Jones (12–6) potentials between the Ar and water molecules, with parameters $\varepsilon = 0.015$ eV and $\sigma = 3.0$ Å taken from Brooks et al. [36]. These parameters yield a well depth and minimum energy intermolecular separation in good agreement with ab initio results [37]. All intermolecular potentials are multiplied by a switching function which smoothly adjusts the intermolecular forces to zero for separations larger than 10 Å. This potential energy surface gives Ar–crystalline ice scattering distributions and collisional energy transfer that are in good agreement with experiment [23,27].

3.2. Simulation conditions

The crystalline ice Ih structure was constructed from the $3 \times 2 \times 2$ Hayward and Reimers unit cell [27,38]. An 'infinitely' large ice surface was modelled by an ice slab containing eight unit cells, with periodic boundary conditions

in the basal (0 0 0 1) surface plane. The $27.04 \times 31.22 \times 29.44$ Å^3 slab consisted of eight bilayers with 96 water molecules in each bilayer. The atomic positions of the molecules in the bottom two bilayers were kept fixed (to maintain the bulk Ih structure) and those in the upper six bilayers were thermalised to 110 K. The motion of the water molecules in the lowest movable bilayer was integrated using the Langevin Equation [27,39] and the dynamics of the remaining water molecules was integrated using a modified Verlet algorithm [40], with an integration step size of 6 fs. In the absence of coupling to the bulk, this gave energy conservation to four significant figures over a 20 ps trajectory.

Low density amorphous (LDA) and high density amorphous (HDA) ice structures were constructed in a similar manner to that used by Wilson et al. [41]. The LDA surface was constructed by depositing randomly orientated water molecules, initially 10 Å above the surface, on a crystalline ice surface that was maintained at 110 K. A total of 576 water molecules (which is effectively six bilayers) were deposited. The HDA surface was constructed by heating these 576 deposited water molecules to 300 K for 500 ps, before thermalising at 110 K for 100 ps. Although LDA and HDA surfaces are not expected to accurately mimic the amorphous surface built experimentally, they are intended to provide two extreme situations – very low density and very high density amorphous ice.

A crystalline surface that contains a ledge was constructed by adding half a bilayer to the crystalline surface, and then thermalising at 110 K. It is important to note that none of the surfaces (crystal, LDA, HDA or ledge) lost their structure during simulations of collisions by Ar.

Ar–ice collisions were simulated by initially placing the Ar ≈ 10 Å above the thermalised ice surface. For the crystalline, LDA and HDA surfaces the Ar x and y coordinates (i.e., in the plane of the surface) were selected from a uniform random distribution $0 \leqslant x \leqslant 27.04$ Å and $0 \leqslant y \leqslant 31.22$ Å, with $z = 10$ Å. For the ledge, only the x coordinate was chosen from a uniform random distribution $0 \leqslant x \leqslant 27.04$ Å, and the y coordinate was set so that the Ar impacted at $v_z = -\sqrt{2E_i/m}\cos\theta_i$, where $E_i = 0.43$ eV is the initial kinetic energy, $m = 39.95$ g mol^{-1} is the Ar mass and $\theta_i = 70°$ is the incident collision angle.

Ensembles of over 20,000 trajectories were run for each surface to ensure statistical convergence. Heating of the ice over multiple collisions was prevented by thermalising the ice for 0.5 ps between collisions. Trajectories were terminated once the Ar atom had either scattered (the Ar–ice separation was 10 Å) or had been thermally trapped on the surface [27]. The Ar atom was considered to be trapped when the magnitude of its velocity was thermal and when its total energy (kinetic + Ar–ice potential energy) was less than the desorption energy. Under these conditions the Ar has thermalised on the surface and requires energy transferred from the surface to desorb. Ar thermalisation was tested by comparing its kinetic energy, averaged over 0.5 ps intervals, with the kinetic energies of the water mol-

ecules in the top bilayer, averaged over the same time interval. When the Ar kinetic energy fell within the water thermal fluctuations, given by the range of kinetic energies of the water molecules in the top bilayer, it was considered to be thermalised. The total energy criterion was also based on the energy averaged over 0.5 ps intervals. By comparing with long time (20–50 ps) trajectories, it has earlier been established that these criteria are necessary and sufficient to identify scattered and trapped trajectories [27].

Collisional energy transfer was determined from $\Delta E_{\text{coll}} = E_i - E_f$, where $E_i = 0.43$ eV is the initial energy of the Ar atom and E_f is its energy after scattering. The in-plane scattering angle relative to the surface normal direction is:

$$\theta_f = \tan^{-1}\left(\frac{v_{y,f}}{v_{z,f}}\right), \tag{1}$$

where $v_{y,f}$ is the velocity of the scattered Ar in the y-direction and $v_{z,f}$ is its velocity in the z-direction.

4. Results and discussion

The experimental data consist of angular-resolved time-of-flight data measured for Ar colliding with amorphous and crystalline ice surfaces. The use of a kinetic energy of 0.43 eV results in a reasonably high fraction of inelastic scattering compared to trapping–desorption, and the large incident angle of 70° is expected to enhance the effects of surface corrugation on the scattering results.

Fig. 1 shows time-of-flight spectra of argon scattering from crystalline and amorphous ice at 110 K. The spectra for crystalline ice on the left side of Fig. 1 show a sharp and fast peak on top of a broader and slower component. The relative size of the two components changes substantially with scattering angle. The fast peak dominates at large scattering angles (in the forward scattering direction), while the slow component increases when moving towards the surface normal direction. The distributions for $\theta_f < 0°$ are essentially the results expected for thermal desorption from a 110 K ice surface. The results for amorphous ice (right-hand side in Fig. 1) show a considerably smaller fast peak compared to the slower one. The intensity of the slow component is also higher in the backward scattering direction compared to the data for crystalline ice.

Data of the type shown in Fig. 1 have been fitted by a sum of two components corresponding to trapping–desorption and direct inelastic scattering. The velocity distribution for thermally desorbed atoms is described by,

$$F_{\text{TD}}(v) = c_1 v^2 \exp\left(-mv^2/2k_B T_1\right) \tag{2}$$

where v is the velocity, c_1 is a scaling factor, m is the argon mass, and T_1 is the temperature. The velocity distribution of the inelastically scattered atoms has the following form:

$$F_{\text{IS}}(v) = c_2 v^2 \exp\left(-m(v - v_0)^2/2k_B T_2\right), \tag{3}$$

where c_2 is a scaling factor, v_0 is a drift velocity and T_2 is a temperature describing the width of the velocity distribution. The distributions take into account that the mass
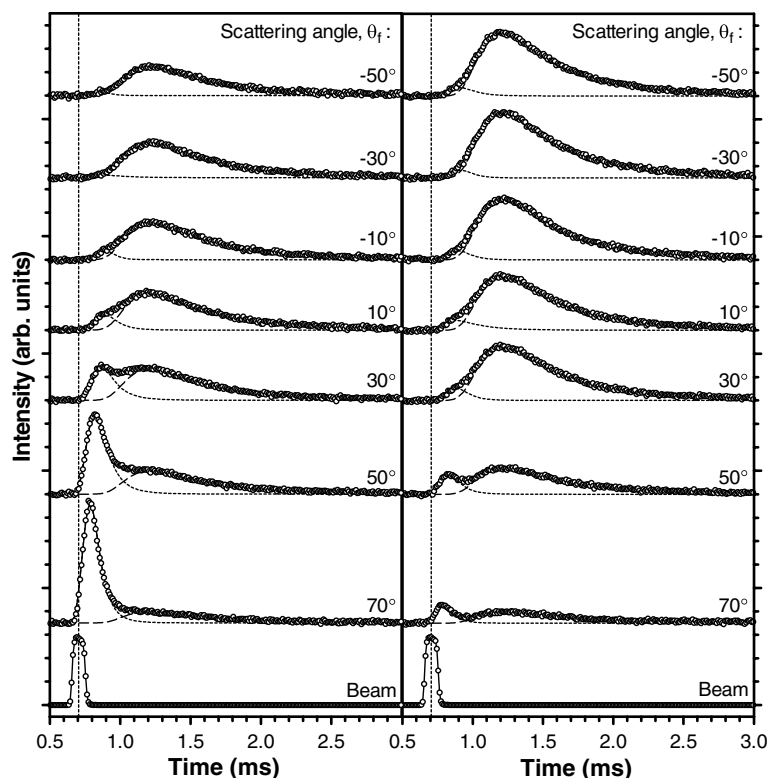
Fig. 1. Time of flight spectra for Ar scattering from crystalline (left) and amorphous (right) ice: experimental data (○), and calculated distributions using Eqs. (2) and (3) for an inelastic (···) and a trapping–desorption (- - -) component, and for the sum of the two components (——). The surface temperature was 110 K, the incident energy 0.43 eV, and the incident angle 70°. The scattering angles are indicated in the figure. The beam measurement was obtained by moving the surface out of the beam and corresponds to elastic scattering.

spectrometer is density sensitive. The sum of Eqs. (2) and (3) has been fitted to the experimental results by changing c_1, c_2, v_0, and T_2, while T_1 is kept constant at the surface temperature. The beam intensity profile at the surface has a width of about 100 μs and this has also been taken into account by performing a convolution over the beam profile. The fitted distributions obtained from Eqs. (2) and (3) and their sum are included in Fig. 1, and the excellent agreement between fits and experimental data is typical for all conditions used in this paper.

The fits to time-of-flight spectra have been used to construct angular distributions for the direct scattering and trapping–desorption channels, and the resulting angular distributions are shown in Fig. 2. The distributions have also been recalculated into a flux in order to compare with the results from MD simulations (see below). The angular distributions for crystalline ice are comparable to the results in earlier molecular beam studies [23]. The angular distribution for thermally desorbed atoms is as expected cosine-like. The distribution for directly scattered atoms peaks close to the specular direction, but is broad and extends towards the surface normal direction due to energy transfer between the Ar atoms and the ice surface. Fig. 2 also shows the average kinetic energy of the inelastically scattered atoms. The atoms lose 50–80% of their incident energy during surface contact, and energy transfer depends sensitively on the scattering angle. The fastest atoms recoil

at angles close to the surface tangential direction and the final kinetic energy then decreases when going towards the surface normal direction, indicating that atoms do not conserve momentum parallel to the surface. The angular distributions observed from amorphous ice are substantially different from those for crystalline ice. The inelastic scattering distribution has a lower intensity. It is also considerably broader and extends into the backward direction. The intensity for the trapping–desorption channel does not show the expected cosine-like distribution. Instead the flux increases as the final angle approaches the incident beam angle. The distribution for the average kinetic energy of the inelastic scattering channel is qualitatively similar to the results for crystalline ice. It is clear that the angular distributions of both scattered and desorbed Ar are sensitive to changes of the properties of the ice surface, and the data indicate that Ar collisions, at least qualitatively, can be used as a probe of the surface structure. Final kinetic energy distributions are on the other hand less sensitive to changes in the ice surface.

Comparison with MD simulations of Ar collisions with different types of ice surfaces helps to provide a mechanistic understanding of the experimental findings, i.e., the decrease in scattering intensity from the amorphous surface and the onset of (increase in) backscattering. Fig. 3 shows side-views of the four different types of surfaces used in the simulations. The crystal structure is clearly seen for the
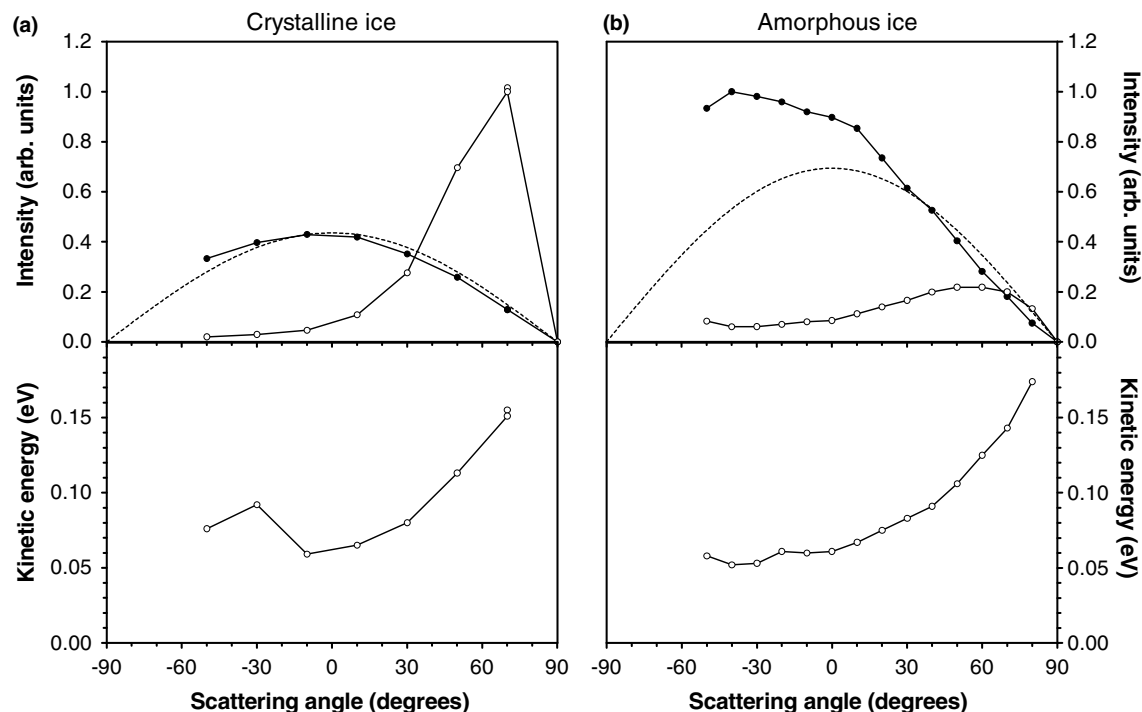
Fig. 2. Ar interactions with crystalline (left) and amorphous (right) ice. (a) Angular distributions for thermal desorption (●) and inelastic scattering (○). A cosine distribution (- - -) is included for comparison. (b) Average kinetic energy of the inelastically scattered atoms. The conditions are the same as in Fig. 1.
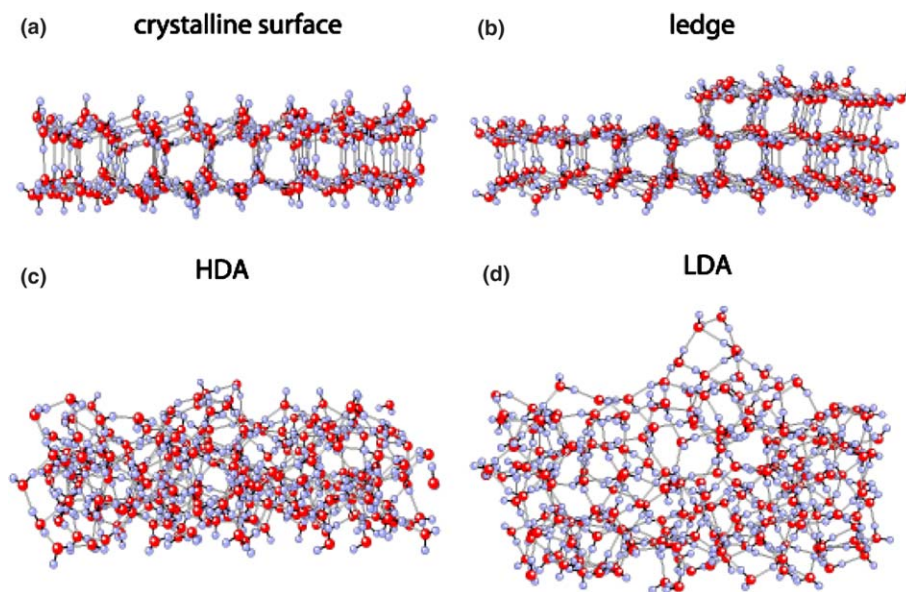

Fig. 3. Side-view snapshots of the upper surface layers in MD simulations of (a) crystalline ice, (b) ice surface with ledge, (c) high density amorphous ice, and (d) low density amorphous ice.

crystalline surface without and with a ledge, while the amorphous surfaces are disordered with different degrees of corrugation depending on the ice density. The density of the four types of surfaces at 0 K is shown in Fig. 4. The density of the crystalline models is set by the potential energy surfaces and constraints used in the calculations. The top-most molecular layers of HDA ice have a density that is higher than crystalline ice and similar to the density of liquid water. The LDA ice instead has a low density of only about 0.5 g cm^{-3}.

In Fig. 5, MD simulations are compared with experimental results for Ar (0.43 eV) scattering from the ice surface (110 K) with $\theta_i = 70°$. The thermally equilibrated atoms in the simulations are not included in the results in Fig. 5, since the trajectories are stopped when the argon atoms are trapped on the surface. Of the total number of
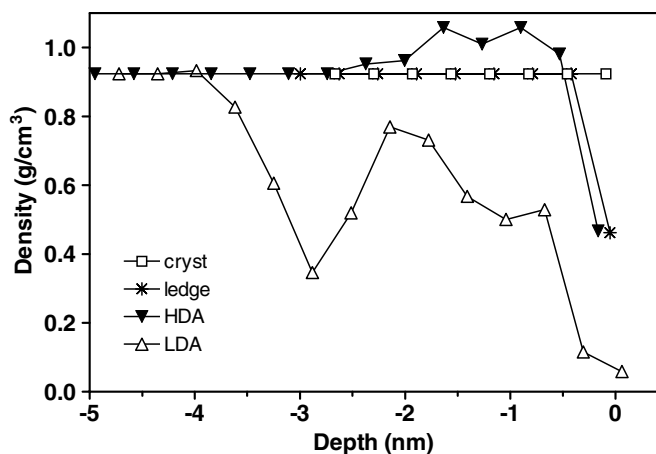
Fig. 4. Calculated ice density as a function of depth from the surface for the different ice surface models studied: crystalline ice (□), HDA ice (▼), LDA ice (△) and crystalline ice with a ledge (∗).
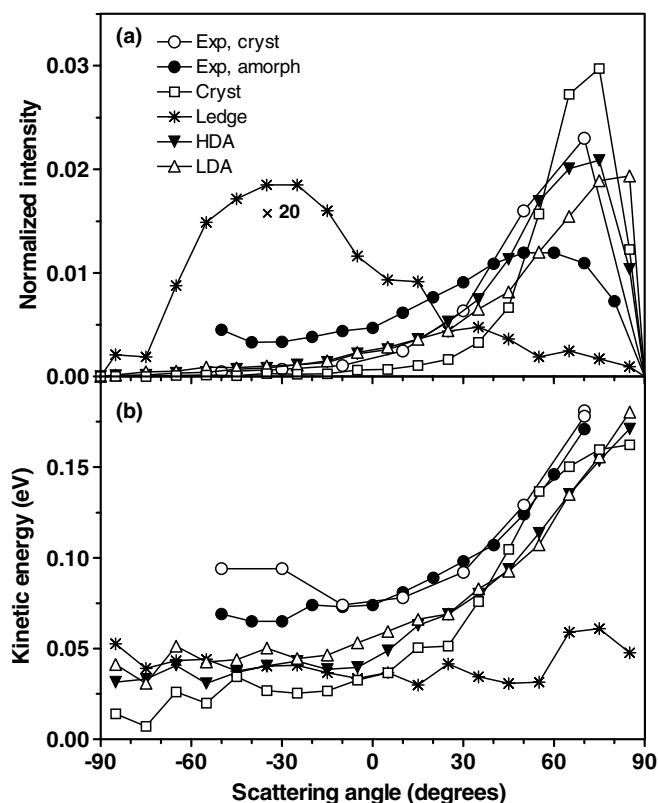

Fig. 5. Calculated angular (a) and average kinetic energy (b) distributions of inelastically scattered atoms for crystalline ice (∗), HDA ice (□), LDA ice (▼) and crystalline ice with a ledge (△). Experimental data for crystalline (○) and amorphous (●) ice are included for comparison. The surface temperature was 110 K, the incident energy 0.43 eV, and the incident angle 70°.

tion for crystalline ice is relatively broad and peaks around the specular scattering direction, but the distribution extends all the way to the surface normal direction. The distribution for HDA ice is broader than for crystalline ice and extends well into the backward direction. A broad distribution is also observed for LDA ice, but in this case the peak shifts towards the tangential direction of the surface. As mentioned above, there is relatively little scattering from the ledge (the data in Fig. 5a is magnified 20-fold), and the distribution is significantly shifted to a backward scattering angle of about −30°.

In agreement with the experimental results, the simulations show that there is more scattering towards the surface normal direction from the amorphous surfaces compared to the crystalline surface. The experimental data for crystalline ice are better described by the simulations for HDA ice than for the simulated crystalline ice, since the simulations do not yield the peak broadening towards the surface normal direction (this may be due to inaccuracies in the potential energy surface or to the fact that the experimental ice surface deviates from a perfect crystal). Taking the difference between simulation and experimental data (based on crystalline surfaces) into account, it is clear that the experimental scattering peak from the amorphous surface is rather well reproduced by the simulated data from the HDA surface (i.e., when the HDA surface is shifted towards the surface normal). However, the increase in back-scattering observed experimentally is not seen in the simulated HDA (or LDA) data, and is only obtained when one has a significant, nanometer-scale corrugation of the ice surface (e.g., as in the idealized ledge surface). It appears that the experimental scattering from amorphous ice is thus best described by a combination of the simulated ledge and HDA amorphous ice data.

The simulated final energy distributions in Fig. 5b also show the same trend as the experimental data, with a decrease in energy when moving towards the surface normal direction. The results for crystalline, HDA and LDA ice are very similar. The simulations also agree qualitatively with experimental data for both crystalline and amorphous ice, but the simulations overestimate the energy transfer for all scattering angles. The results for the ledge surface are very different from the rest of the data with a final energy of about 0.05 eV independent of scattering angle, and the atoms have thus lost about 90% of their initial energy.

We have not attempted to refine the potential energy surface used in the simulations to obtain a better agreement with the experimental data, and quantum effects cannot be ruled out as a cause for the deviations between theory and experiments. Some of the disagreement between experiments and simulations may also be explained by deviations from a crystal surface in the experiments. The simulations show that the angular distributions change gradually when going from crystalline, to HDA, and to LDA ice, which indicates that Ar scattering is not very sensitive to the detailed microscopic structure of the surface. Comparison between experimental data and simulations indicate that

trajectories, about 25% scattered inelastically from the crystalline, HDA and LDA surfaces, while only 2% scattered from the ledge. As seen in Fig. 5a, the simulated angular distributions for crystalline, LDA and HDA ice show the same qualitative features. The simulated distribu-

a large (nanometer-scale) surface corrugation on the amorphous ice surface is required for back-scattering, but that a high density amorphous surface may explain the general shift in scattering toward the surface normal direction. The amorphous layer was deposited at 110 K and considering the relatively high mobility of water at this temperature it is not surprising that the surface may have a structure similar to the simulated HDA structure. However, nanometer-scale surface corrugations are required for backscattering and we conclude that ledges and mismatches with dimensions larger than the size of individual water molecules are frequent on the amorphous surface.

The angular distribution observed for the trapping–desorption channel on amorphous ice deviates substantially from the cosine distribution since it shows a large backscattering component. If Ar diffusion on the amorphous ice surface is on the same time scale, or slower than desorption, then this is probably due to the fact that Ar ($\theta_i = 70°$) preferentially adsorbs – and hence desorbs – on 'backscattering' sides of surface corrugations. In addition, MD simulations show very low kinetic energies in the backward direction, and a fraction of the flux identified as trapping–desorption may in fact be due to direct scattering with a low final energy. The flux is, however, large and it seems likely that it is dominated by a backward directed emission of a trapping–desorption channel. This effect again indicates that large scale corrugation dominates the outcome of the Ar–ice interactions.

In earlier studies Al Halabi et al. carried classical trajectory calculations of H [42] and CO [43] collisions with crystalline and amorphous ice. A lower sticking probability was observed for H on amorphous ice than on crystalline ice, and the difference was attributed to a surface topography with many sites being less suitable for adsorbing the incoming H atom on the amorphous surface. CO–ice calculations were performed for normal incidence. Energy transfer from the impinging molecule to the crystalline and the amorphous surface was found to be quite efficient, and trapping probabilities were comparable on the two types of surfaces. Collisions with amorphous ice also resulted in a wider angular distribution of scattered molecules than for crystalline ice. Their calculated average density of the amorphous ice was about 0.93 g cm^{-3}, and the surface properties were likely somewhere in between the properties of HDA and LDA ice in the present study. We conclude that the earlier results for CO agree well with the present results. The trapping probabilities were similar for Ar on crystalline, HDA and LDA ice and the angular distribution of scattered atoms becomes broader when going from crystalline to amorphous ice. The different choices of incident angles and energies preclude a more detailed comparison between the two studies.

5. Conclusions

The results show that the Ar–ice collisions are highly inelastic and that trapping–thermal desorption is the dominating outcome, confirming the earlier results for argon scattering from crystalline ice [23]. Energy loss to the surface is large both perpendicular and parallel to the surface plane. The experimental results for amorphous and crystalline ice are significantly different. The trapping probability is higher on amorphous ice and the angular distributions are also very different for the two cases. Molecular dynamics simulations show qualitative, and in some cases semi-quantitative, agreement with the experimental energy transfer data and angular distributions. In addition to the fundamental importance of the results, it is concluded that argon scattering may be used to probe changes in surface structure on the nanometer length-scale, and it may thereby complement other techniques for studies of structural changes of complex surfaces.

References

[1] P. Jenniskens, D.F. Blake, Science 265 (1994) 753.
[2] R.H. Brown, D.P. Cruikshank, Annu. Rev. Earth Planet. Sci. 25 (1997) 243.
[3] L.J. Allamandola, S.A. Sandford, G.J. Valero, Icarus 76 (1988) 225.
[4] E. Mayer, R. Pletzer, Nature (Lond.) 319 (1986) 298.
[5] A.H. Narten, C.G. Venkatesh, S.A. Rice, J. Chem. Phys. 64 (1976) 1106.
[6] K.P. Stevenson, G.A. Kimmel, Z. Dohnalek, R.S. Smith, B.D. Kay, Science 283 (1999) 1505.
[7] G.A. Kimmel, K.P. Stevenson, Z. Dohnalek, R.S. Smith, B.D. Kay, J. Chem. Phys. 114 (2001) 5284.
[8] G.A. Kimmel, Z. Dohnalek, K.P. Stevenson, R.S. Smith, B.D. Kay, J. Chem. Phys. 114 (2001) 5295.
[9] Z. Dohnalek, G.A. Kimmel, P. Ayotte, R.S. Smith, B.D. Kay, J. Chem. Phys. 118 (2003) 364.
[10] P. Parent, C. Laffon, C. Mangeney, F. Bournel, M. Tronc, J. Chem. Phys. 117 (2002) 10842.
[11] B. Rowland, J.P. Devlin, J. Chem. Phys. 94 (1991) 812.
[12] N. Horimoto, H.S. Kato, M. Kawai, J. Chem. Phys. 116 (2002) 4375.
[13] Z. Dohnalek, G.A. Kimmel, R.L. Ciolli, K.P. Stevenson, R.S. Smith, B.D. Kay, J. Chem. Phys. 112 (2000) 5932.
[14] A. Bar-Nun, G. Herman, D. Laufer, M.L. Rappaport, Icarus 63 (1985) 317.
[15] M.P. Collings, J.W. Dever, H.J. Fraser, M.R.S. McCoustra, D.A. Williams, Astrophys. J. 583 (2003) 1058.
[16] V. Sadtchenko, K. Knutsen, C.F. Giese, W.R. Gentry, J. Phys. Chem. B 104 (2000) 2511.
[17] V. Sadtchenko, K. Knutsen, C.F. Giese, W.R. Gentry, J. Phys. Chem. B 104 (2000) 4894.
[18] B. Rowland, M. Fisher, J.P. Devlin, J. Chem. Phys. 95 (1991) 1378.
[19] H.G. Hixson, M.J. Wojcik, M.S. Devlin, J.P. Devlin, V. Buch, J. Chem. Phys. 97 (1992) 753.
[20] M.T. Sieger, T.M. Orlando, Surf. Sci. 390 (1997) 92.
[21] W.C. Simpson, M.T. Sieger, T.M. Orlando, L. Parenteau, K. Nagesha, L. Sanche, J. Chem. Phys. 107 (1997) 8668.
[22] E. Vichnevetski, A.D. Bass, L. Sanche, J. Chem. Phys. 113 (2000) 3874.
[23] P.U. Andersson, M.B. Någård, K. Bolton, M. Svanberg, J.B.C. Pettersson, J. Phys. Chem. A 104 (2000) 2681.

[24] P.U. Andersson, M.B. Någård, J.B.C. Pettersson, J. Phys. Chem. B 104 (2000) 1596.

[25] M.T. Suter, P.U. Andersson, J.B.C. Pettersson, Phys. Scripta T110 (2004) 350.

[26] P.U. Andersson, M.B. Någård, G. Witt, J.B.C. Pettersson, J. Phys. Chem. A 108 (2004) 4627.

[27] K. Bolton, M. Svanberg, J.B.C. Pettersson, J. Chem. Phys. 110 (1999) 5380.

[28] K. Bolton, J.B.C. Pettersson, Chem. Phys. Lett. 312 (1999) 71.

[29] M.T. Suter, P.U. Andersson, J.B.C. Pettersson (to be submitted).

[30] N.J. Sack, R.A. Baragiola, Phys. Rev. B48 (1993) 9973.

[31] M.S. Westley, G.A. Baratta, R.A. Baragiola, J. Chem. Phys. 108 (1998) 3321.

[32] D.R. Haynes, N.J. Tro, S.M. George, J. Phys. Chem. 96 (1992) 8502.

[33] W.L. Jorgensen, J. Chandrasekhar, J.D. Madura, R.W. Impey, M.L. Klein, J. Chem. Phys. 29 (1983) 926.

[34] G.-J. Kroes, Surf. Sci. 275 (1992) 365.

[35] G.-J. Kroes, D.C. Clary, J. Phys. Chem. 96 (1992) 7079.

[36] R. Brooks, F. Kalos, A.E. Grosser, Mol. Phys. 27 (1974) 1071.

[37] F.-M. Tao, W. Klemperer, J. Chem. Phys. 101 (1994) 1129.

[38] J.A. Hayward, J.R. Reimers, J. Chem. Phys. 106 (1997) 1518.

[39] A.E. DePristo, H. Metiu, J. Chem. Phys. 90 (1989) 1229.

[40] M. Svanberg, Mol. Phys. 92 (1997) 1085.

[41] M.A. Wilson, A. Pohorille, P. Jenniskens, D.F. Blake, Origins Life Evol. Biosphere 25 (1995) 3.

[42] A. Al-Halabi, A.W. Kleyn, E.F. van Dishoeck, G.J. Kroes, J. Phys. Chem. B106 (2002) 6519.

[43] A. Al-Halabi, E.F. van Dishoeck, G.J. Kroes, J. Chem. Phys. 120 (2004) 3358.